# Supplementary Information

## Spatially Confined Transition Metals Boost High Initial Coulombic Efficiency in Alloy Anodes

Haoyu Fu[a, ‡], Fangchao Gu[a, ‡], Yize Niu[a, ‡], Shuxuan Liao[a], Zeyuan Bu[a], Haonan Wang[a], Dong Yang[a], Xiaoshan Wang[a]* and Qiang Li[a,b]*

[a] College of Physics, Weihai Innovation Research Institute, College of Materials Science and Engineering, Qingdao University, Qingdao 266071, China

[b] University of Waterloo, Waterloo, Ontario N2L 3G1, Canada.

* Corresponding author E-mail: liqiang@qdu.edu.cn (Q. Li); wangxiaoshan1@qdu.edu.cn (X.S. Wang)

# Contents

# Experimental section

## Preparation of multilayer thin film electrodes

All multilayer film electrodes were deposited on Cu foil substrates ($5 \times 5$ cm$^2$) using a KYKY JGB-560 magnetron sputtering system. The thickness of $SnO_2$, $NiO$, $CoO$, $Fe_2O_3$ and $SiO_2$ are shown in Table S1. Under optimized conditions, in a typical deposition, a radio frequency magnetron (power 90 W, 2.5 Pa Ar as the working gas) was used during deposition after a base pressure of $3.5 \times 10^{-5}$ Pa was achieved.

## Material Characterization

The microstructures were investigated by scanning electron microscopy (SEM, JEOL JSM-7100F) and transmission electron microscopy (TEM, JEOL, JEM-2100F). The valence states of multilayer thin film electrodes were determined with X-ray photoelectron spectroscopy (XPS) on an Axis Ultra DLD spectrometer.

## Electrochemistry Characterization

The half cells were assembled with $NiO/SnO_2$ multilayer films as working electrode, lithium metal foils as counter electrode. A Celgard 2325 film (Whatman) was placed between the working electrodes and the lithium metal. The electrolyte of all coin cells was 1M $LiPF_6$ in 1:1 (volume ratio) ethylene carbonate (EC) and diethyl carbonate (DEC) with 5% fluoroethylene carbonate (FEC). Usually, the electrochemical performance was tested on a Neware Battery Tester system (CT-3008W) within a voltage window of 0.01–3 V. Alternating current impedance of the NSM cells were measured with a frequency range from 100 kHz to 0.01 Hz by a SI 1260 Impedance/Gain-Phase and Solartron SI 1287 Electrochemical Interface Analyzer. The galvanostatic intermittent titration technique (GITT) test was conducted on a Land Battery Tester.

## Magnetic Characterization

The nonmagnetic NSM flexible packaging cells were assembled using the same counter electrode and electrolyte as the coin batteries. Magnetic measurements were performed on a physical property measurement system (PPMS, Quantum Design) using the self-developed batteries for the in-situ measurements. Simultaneously, these batteries were connected in C-V at 0.5 mV s$^{-1}$ from 0.01 to 3 V and

cycled at 300 K, while magnetization was sampled at a constant field (3 T). The background deduction is rigorously conducted during operando magnetometry measurements to exclude signal interference from the cell assembly component.

## Magnetic calculation of grain size

The magnetization of superferromagnetic particles will follow a Langevin function

$$M\ (H, T) = M_0 L(\mu_p H/kT) \tag{1}$$

where $L(x) = \coth x - (1/x)$ and $\mu_p$ is the magnetic moment per particle. Fitting our measured data at 300 K to the Langevin function, we found $\mu_p$ =253.72 $\mu B$. Considering 2 $\mu B$ per Ni atom, an average particle diameter of 1.2 nm could be deduced.

## DFT calculations

All the DFT calculations were performed using the Vienna ab initio simulation packages (VASP). Based on the generalized gradient approximation (GGA), the exchange-correlation term between electrons was described by the Perdew-Burke-Ernzerh (PBE) functional. Brillouin zone integration was accomplished by 2×2×1 Monkhorst-Pack k-point mesh for structural optimizations. The projector-augmented wave method was used to describe the electron-ion interactions and the cut-off energy for the plane wave basis set was 450 eV. The criterion of energy convergence was $1\times10^{-5}$ eV. The optimization was complete until the residual force of each atom was less than 0.05 eV/Å. The dipole moment was calculated parallel to the z direction and a vacuum of 15 Å at the z direction was employed to avoid interactions between periodic images. The calculation of adsorption free energy was defined as the equation: $E_{ads}$ = E(total) − E(surface) − E(isolated adsorbate). The Gibbs free energy (G) can be calculated as the equation: $\Delta G = \Delta E_{ads} + \Delta ZPE - T\Delta S$, where $E_{ads}$ was the electronic adsorption energy in the self-consistent calculation, and ZPE stand for the zero-point energy difference between adsorbed and gaseous species while TS was the entropy correction at 298 K.

# Supplementary Tables and Figures

**Table S1.** Preparation conditions and parameters of the various multilayers.

| Film | Thickness (nm) | Power | Pressure | Others |
|---|---|---|---|---|
| $SnO_2$ | 150nm | 90W | 2.5Pa | Room temperature |
| NiO | 150nm | 90W | 2.5Pa | Room temperature |
| NSM | $NiO$-$SnO_2$ 10nm/5nm (10 cycle) | 90W | 2.5Pa | Room temperature |
| CSM | $CoO$-$SnO_2$ 10nm/5nm (10 cycle) | 90W | 2.5Pa | Room temperature |
| FSM | $Fe_2O_3$-$SnO_2$ 10nm/5nm (10 cycle) | 90W | 2.5Pa | Room temperature |
| $SiO_2$ | 200nm | 90W | 2.5Pa | 550℃ |
| $SiO_2$-NiO | 15nm/5nm (10 cycle) | 90W | 2.5Pa | 550℃ |

**Table S2.** Resistance of $SnO_2$ and NSM in different cycles.

| Resistance($\Omega$) / Cycle Number | $SnO_2$ | NSM |
|---|---|---|
| 1 | 35 | 25 |
| 10 | 45 | 26 |
| 20 | 48 | 28 |
| 30 | 52 | 30 |
| 50 | 93 | 32 |
| 80 | 125 | 31 |
| 100 | 160 | 35 |
| 200 | - - | 42 |
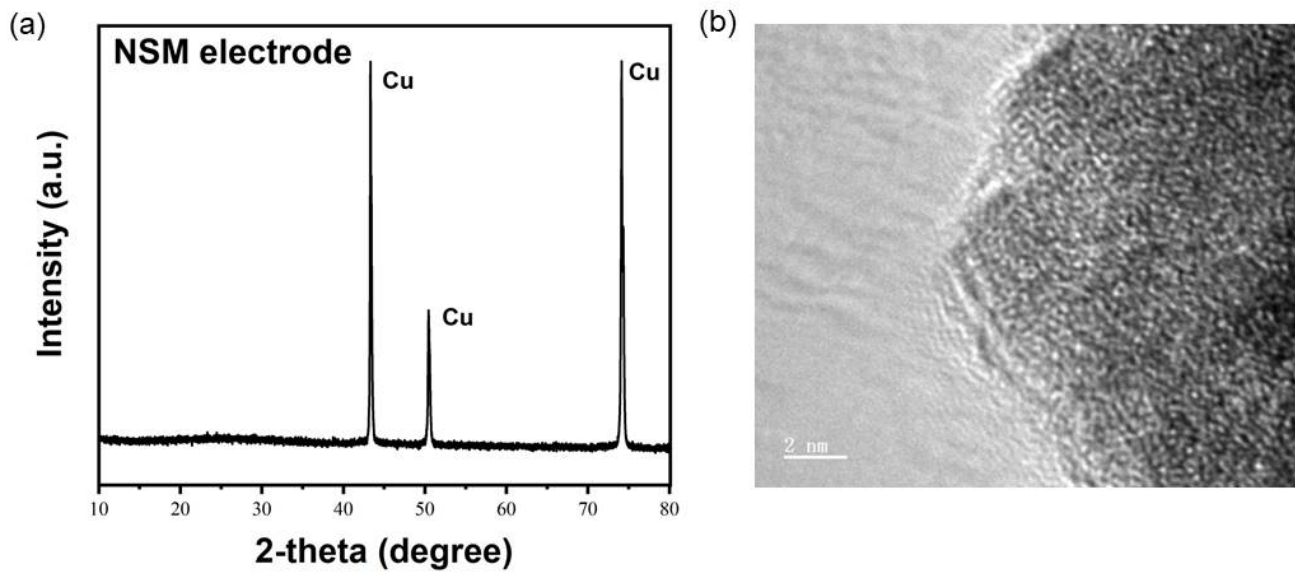
**Figure S1.** (a) XRD pattern of NSM electrode, (b) TEM image of NSM electrode.
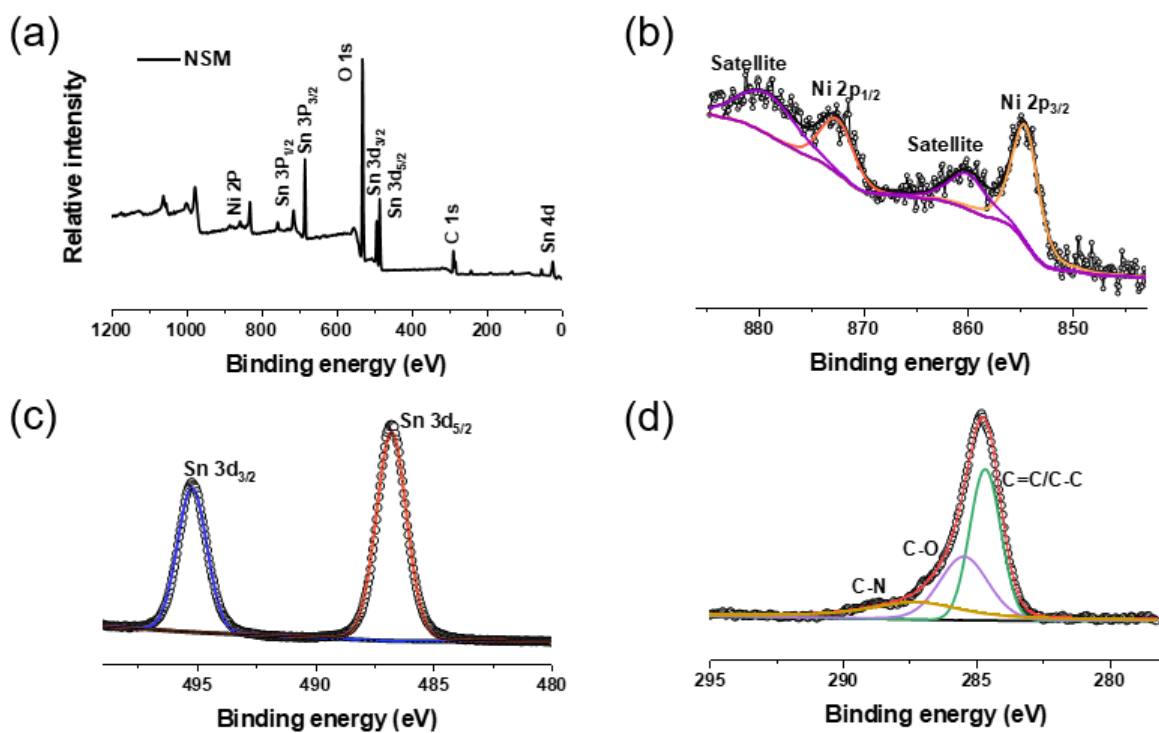
**Figure S2.** (a) XPS survey spectrum of initial NSM electrode. (b) High-resolution XPS of Ni 2p, (c) Sn 3d, (d) C 1s.
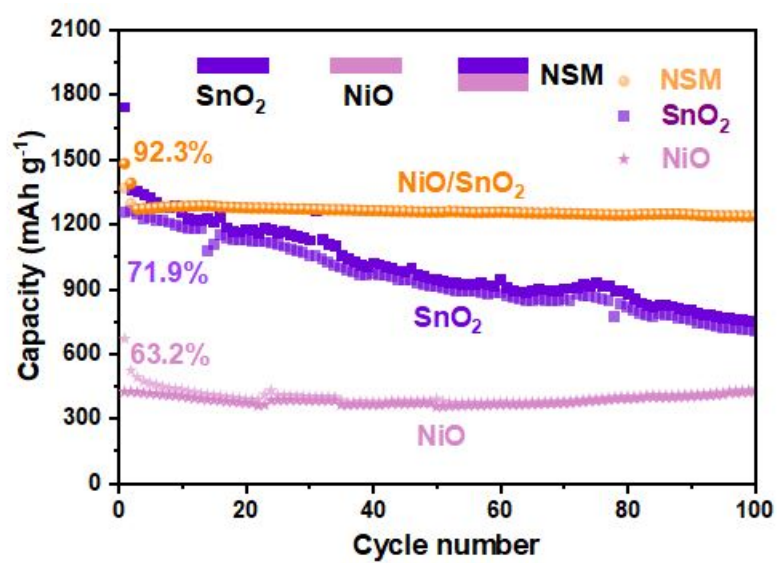
**Figure S3.** ICE and cycling performance in the initial 100 cycles at a current density of 1000 mA g$^{-1}$ for SnO$_2$, NiO and NSM anodes.
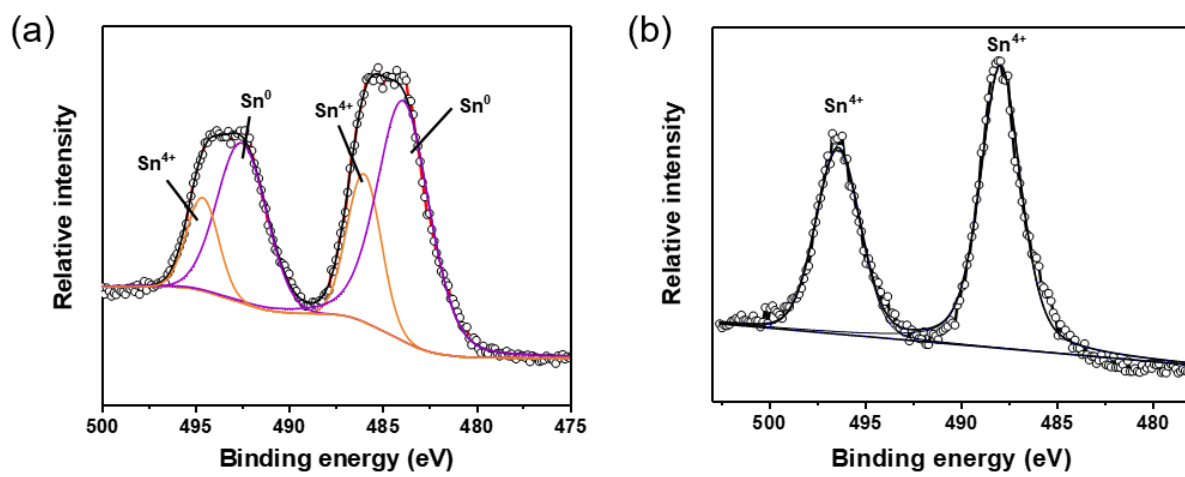
**Figure S4.** High-resolution XPS of Sn 3d for (a) $SnO_2$ and (b) NSM at charging to 3.0V after 50 cycles.
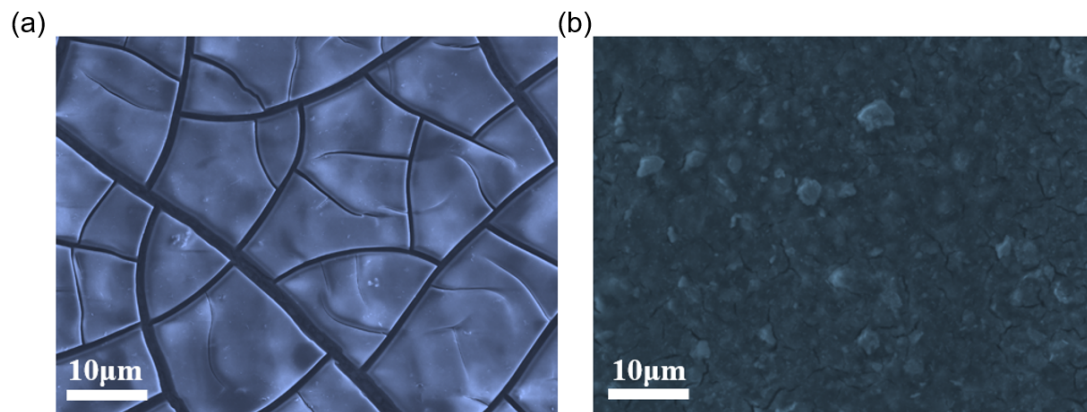
**Figure S5.** SEM images of (a) pure SnO$_2$ and (b) NSM nanocomposite anodes after 50 cycles.
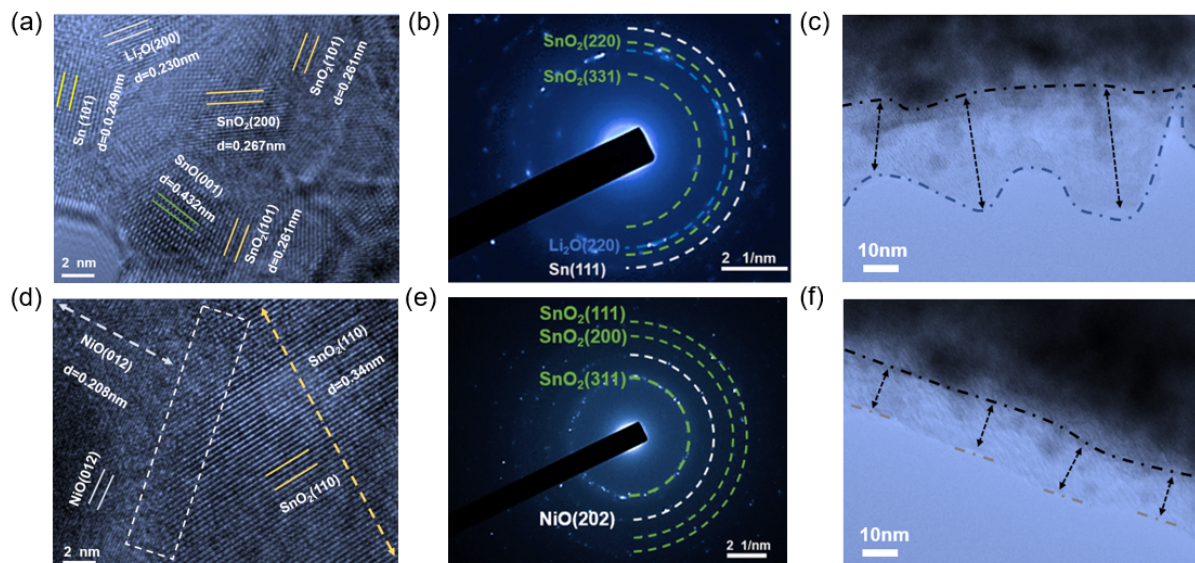
**Figure S6.** Ex situ STEM images of NSM and SnO$_2$ after 50 cycles and charge to 3 V. HRTEM images of (a) SnO$_2$ and (d) NSM. SAED patterns of (b) SnO$_2$ and (e) NSM. SEI patterns of (c) SnO$_2$ and (f) NSM.
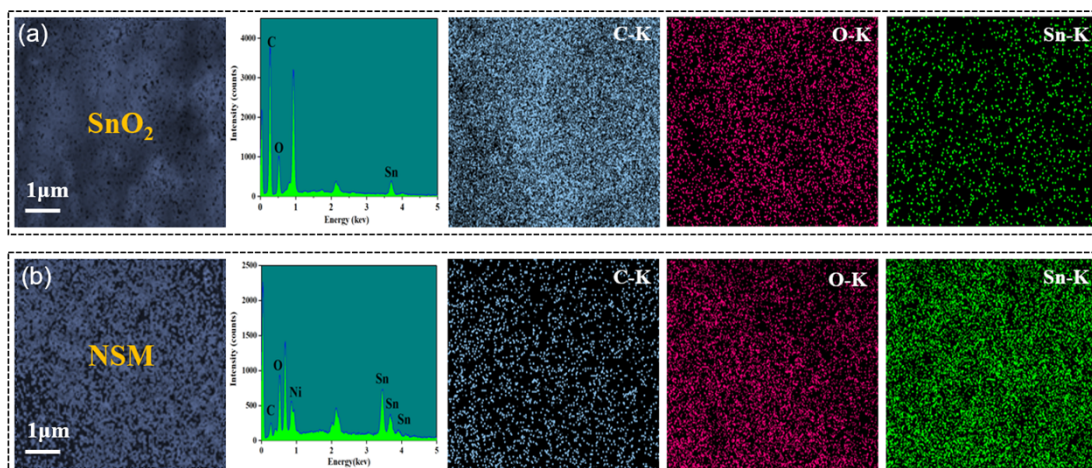
**Figure S7.** EDX mapping of (a) SnO₂ and (b) NSM electrodes after 50 cycles.
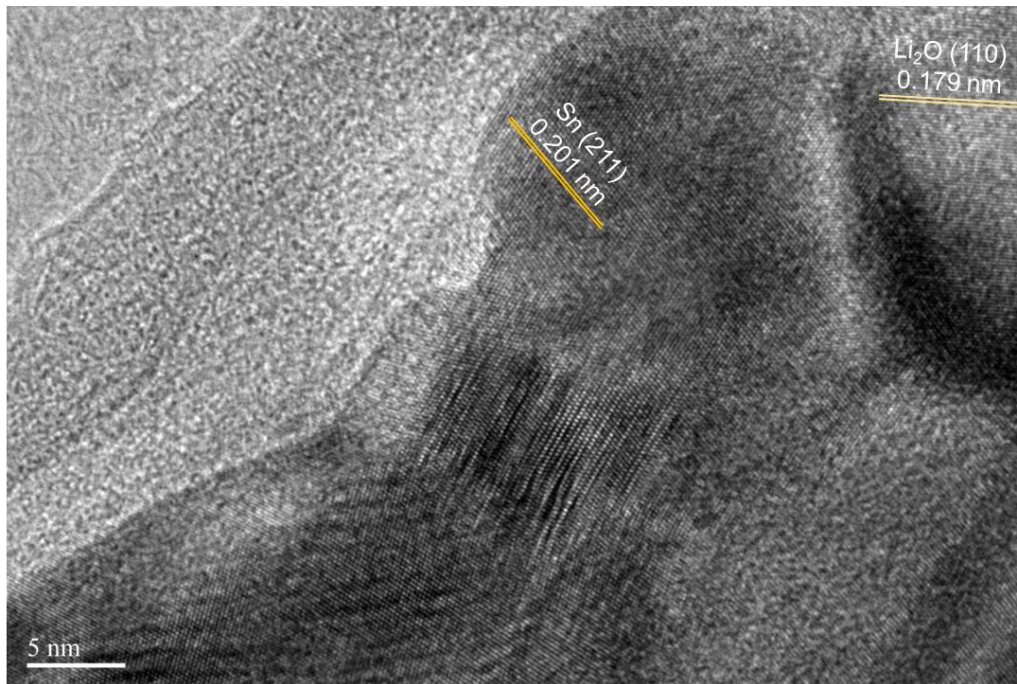
**Figure S8.** Ex situ TEM images of lithiated products of SnO$_2$ electrode after 100 cycles.
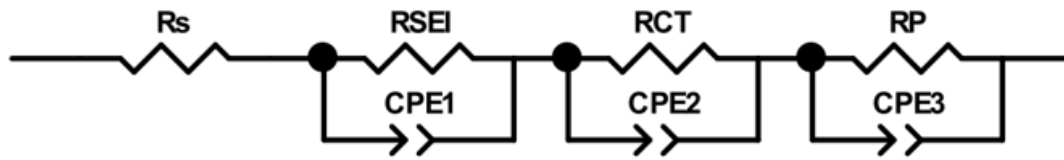
**Figure S9.** Randle equivalent circuit for NSM.
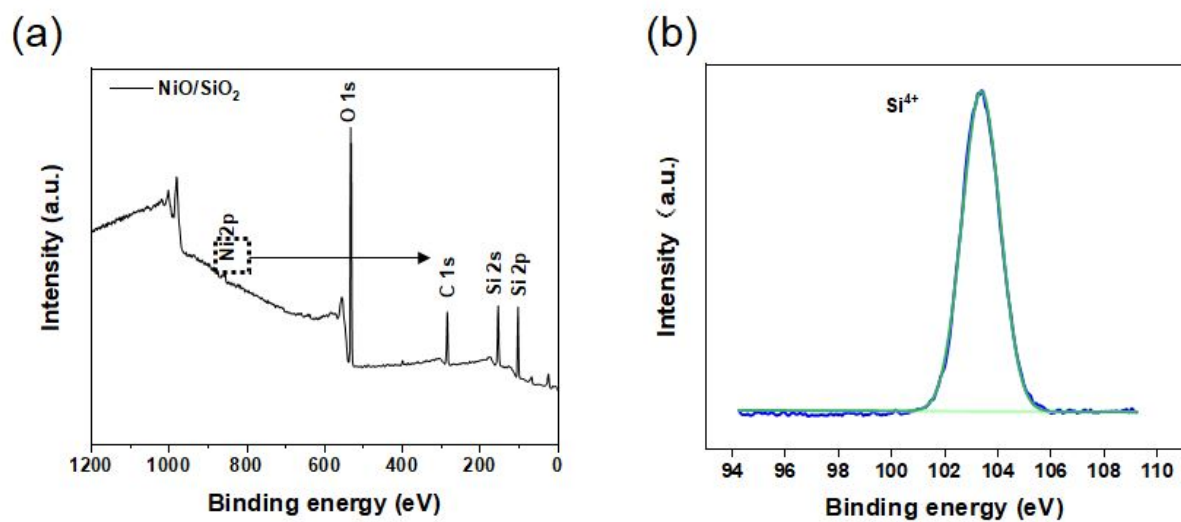
**Figure S10.** XPS survey of (a) initial NiO/SiO$_2$ thin film. (b) The high-resolution Si element.
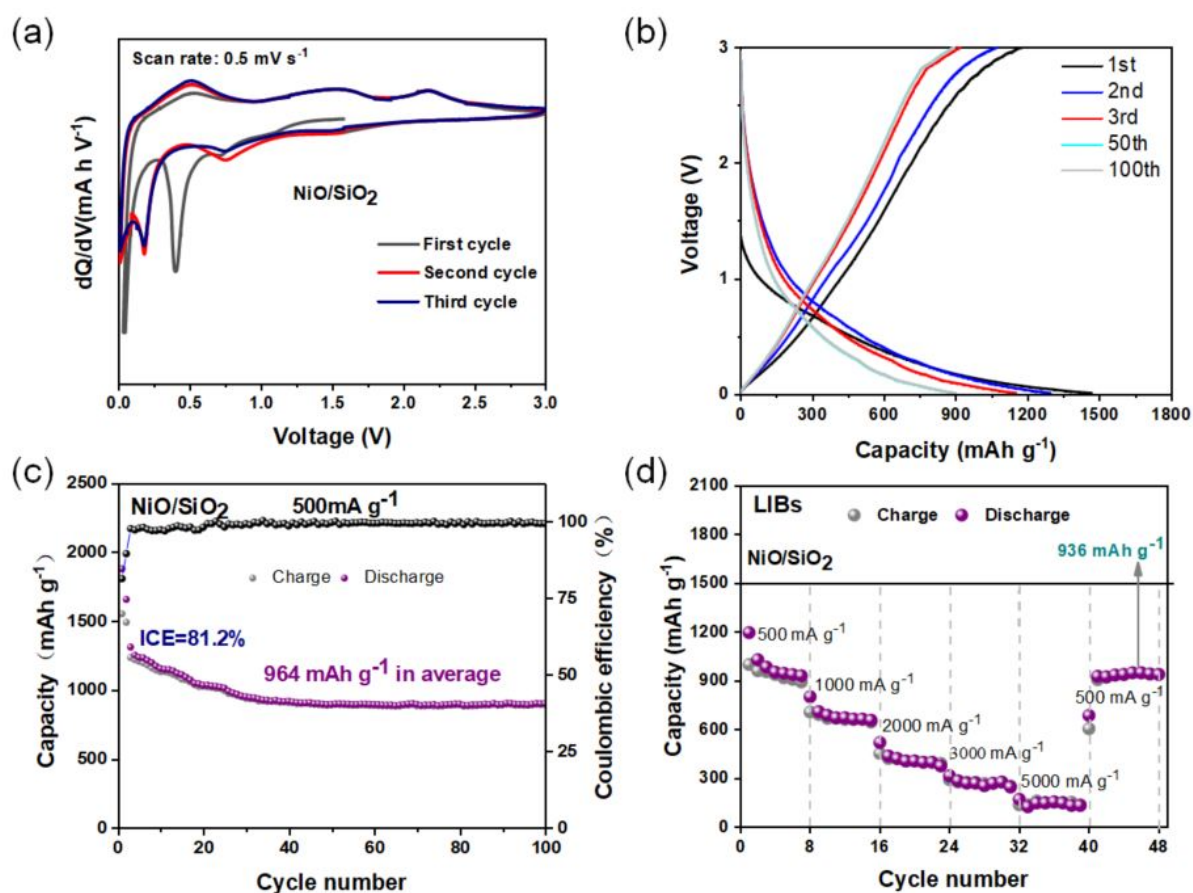
**Figure S11.** Electrochemical characterization and properties of NiO/SiO$_2$ multilayer films. (a) CV curves of a NiO/SiO$_2$ multilayer films electrode for the first three cycles at a scan rate of 0.5 mV s$^{-1}$ over the potential window of 0.01-3 V. (b) Charge-discharge curves of NiO/SiO$_2$ multilayer films. (c) Cycle performance of the NiO/SiO$_2$ multilayer films electrode at 500 mA g$^{-1}$ for LIBs. (d) Rate capabilities of NiO/SiO$_2$ electrodes.

The XPS characterization of NiO/SiO$_2$ is shown in Figure S8, and the peak of 103.8 eV corresponds to the Si$^{4+}$, indicating that highly pure NiO/SiO$_2$ is prepared.[1] The cyclic voltammetry (CV) test at a scan speed of 0.5mV s$^{-1}$ of NiO/SiO$_2$ is shown in Figure S11a and a sharp peak near 0.5 V on the first cathodic scan is caused by the initial reduction of NiO to Ni, the reaction mechanism for SiO$_2$ to storage Li is proposed to include two parts, one is reversible and the other is irreversible. The irreversible reaction is generally written as follows:

$$SiO_2 + 4Li^+ + 4e^- \leftrightarrow Si + 2Li_2O \tag{1}$$

$$SiO_2 + 2Li^+ + 2e^- \leftrightarrow Si + 1/2Li_4SiO_4 \tag{2}$$
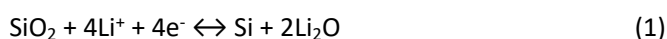
The reversible reaction is usually expressed as:

$$SiO_2 + 4/5Li^+ + 4/5e^- \leftrightarrow Si + 2/5Li_2Si_2O_5 \tag{3}$$

$$Si + xLi^+ + xe^- \leftrightarrow 2Li_xSi \qquad (4)$$

The degree of reconversion dominates ICE and reversible capacity. From the above analysis, the loss of an irreversible $Li_2O$ can be catalytically decomposed by Ni. and reused during the delithiation process which induces an increasing of ICE and superior capacity. An ultrahigh average ICE of 81.2%, with 964 mAh $g^{-1}$ in average capacity after 100 cycles at a current density of 500 mA $g^{-1}$ was achieved as shown in Figure S9b and c, which is far superior to pure $SiO_2$. (Figure S10) And fast kinetics and ion diffusion rate of the $NiO/SiO_2$ multilayers have been reflected as shown in Figure S9d.
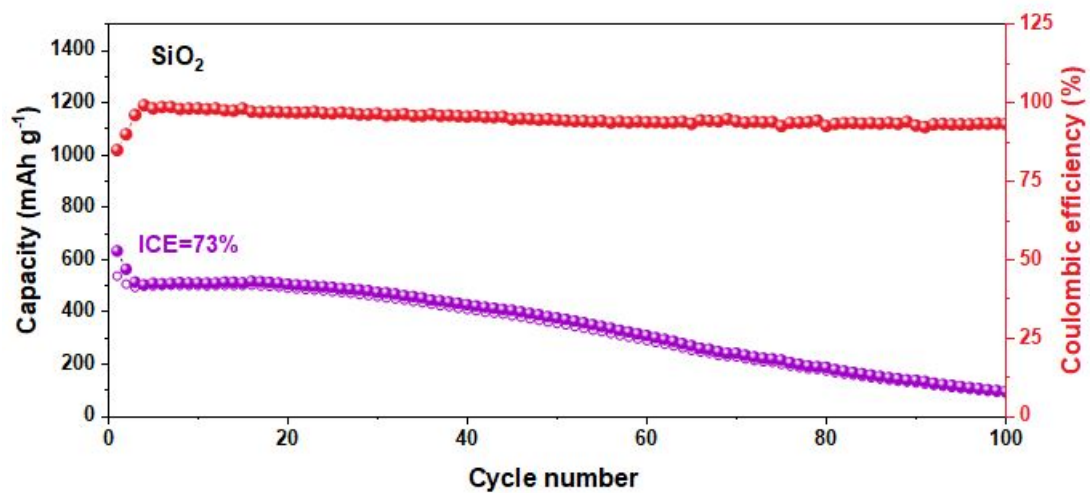
**Figure S12.** Cycle performance of the pure SiO$_2$ electrode at 500 mA g$^{-1}$ for LIBs.
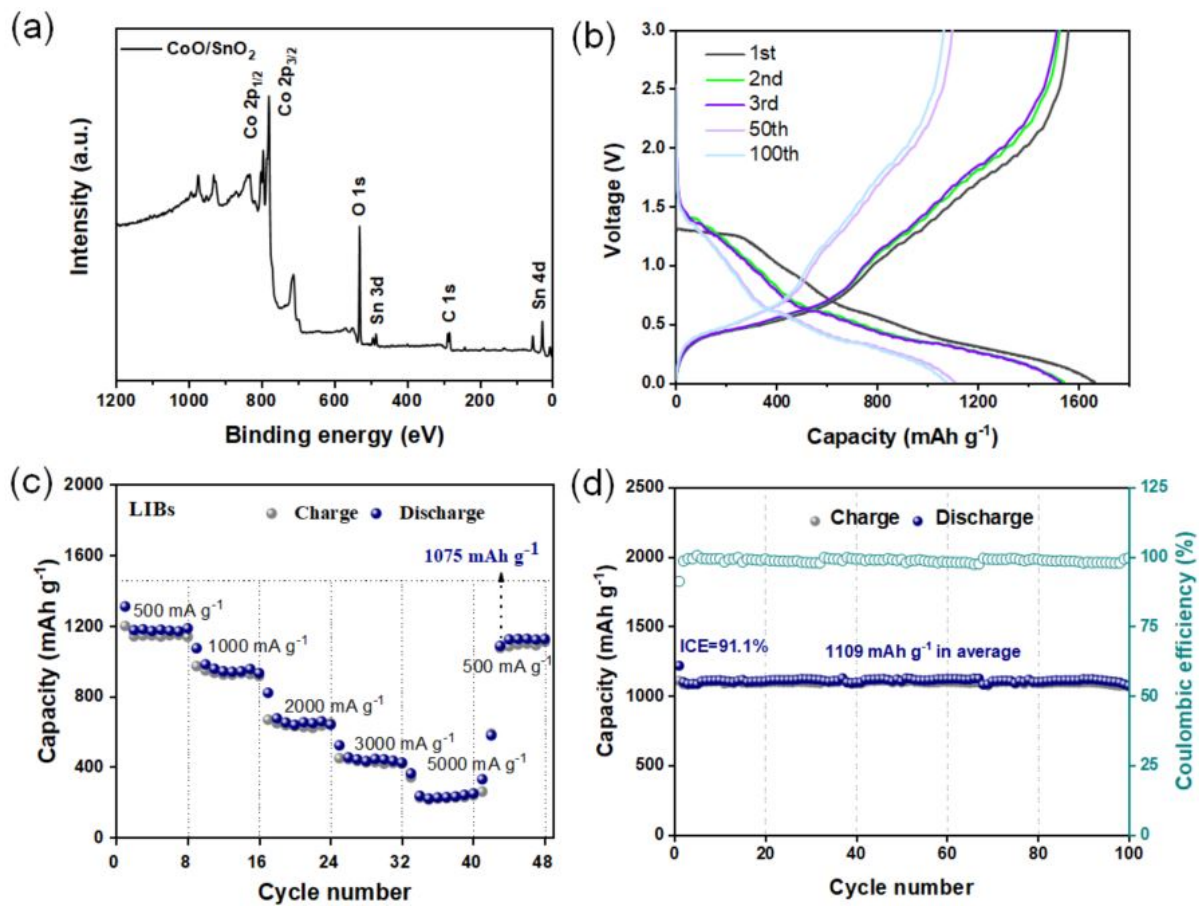
**Figure S13.** (a) XPS survey of CoO/SnO$_2$. (b) Charge-discharge curves of CoO/SnO$_2$ multilayer films. (c) Rate capabilities of CoO/SnO$_2$ electrodes. (d) Cycle performance of CoO/SnO$_2$ multilayer films electrode at 500 mA g$^{-1}$ for LIBs.
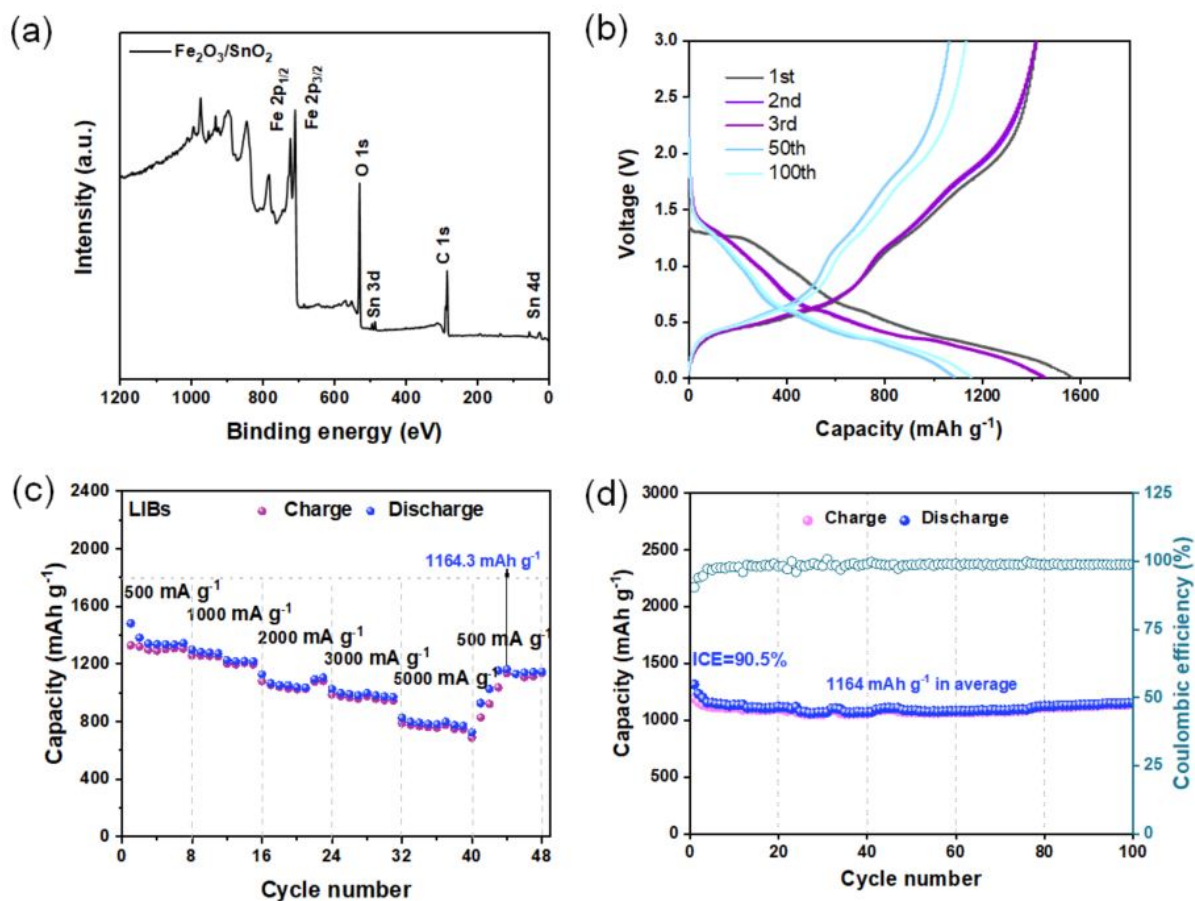
**Figure S14.** (a) XPS survey of $Fe_2O_3/SnO_2$. (b) Charge-discharge curves of $Fe_2O_3/SnO_2$ multilayer films. (c) Rate capabilities of $Fe_2O_3/SnO_2$ electrodes. (d) Cycle performance of $Fe_2O_3/SnO_2$ multilayer films electrode at 500 mA g$^{-1}$ for LIBs.

The XPS characterization of CSM and FSM are shown in Figure S11a and Figure S12a, which indicates that pure CSM and FSM are prepared. Obviously, as expected, ultra-high ICE of FSM (90.5%) and CSM (91.1%) electrodes were achieved. The high capacities of 1109mAh g$^{-1}$ and 1164mAh g$^{-1}$ in the FSM and CSM electrodes at 500 mA g$^{-1}$ and better rate performance were obtained (Figure S11, S12). From the above analysis, it can be seen that TM in situ converted from TMO will significantly improve the ICE and electrochemical performance of the alloy materials of $SnO_2$ and $SiO_2$, implying a novel fundamental strategy to design highly reversible and stable alloy-type electrode materials for large capacity energy storage.[2,3]
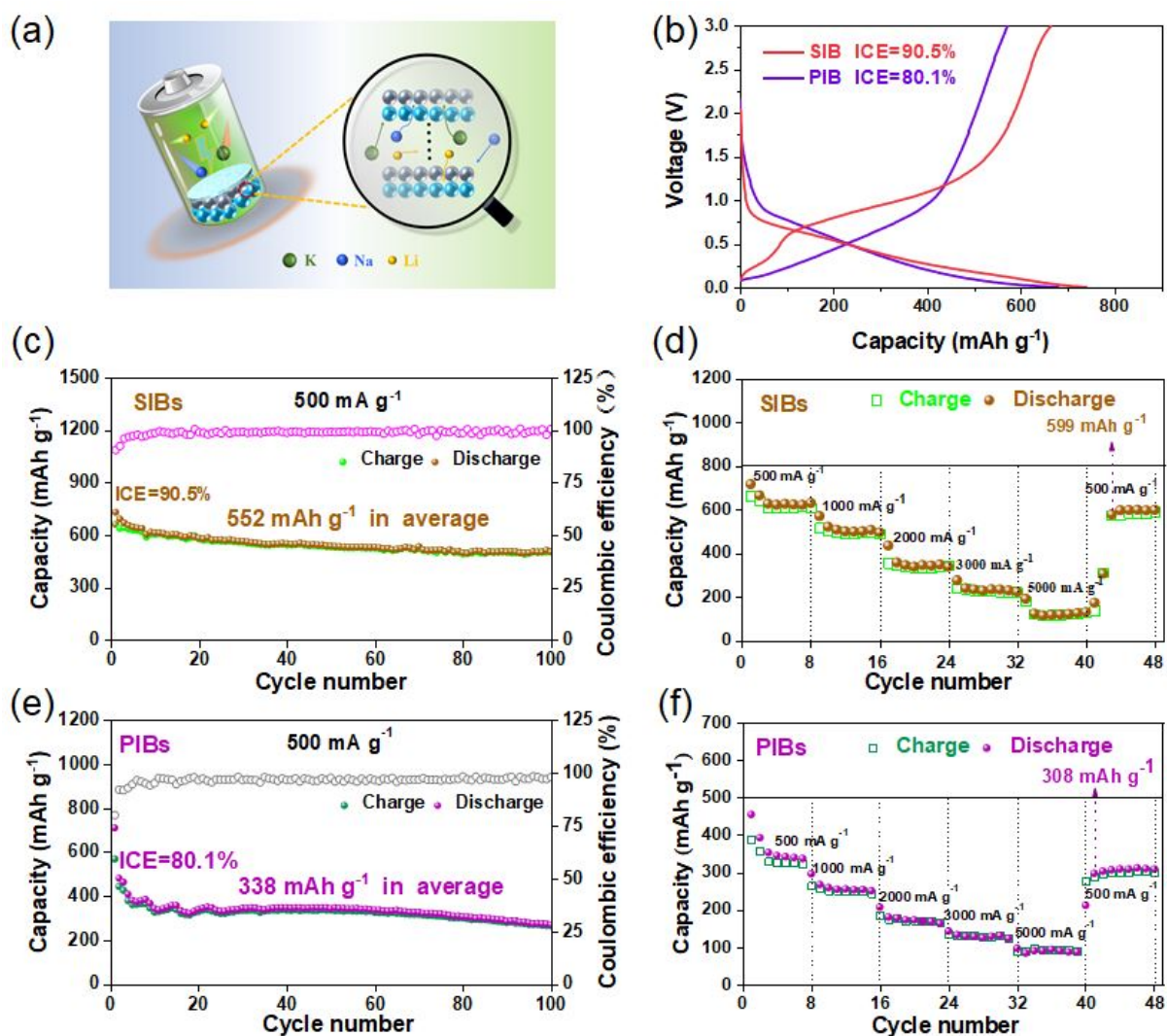
**Figure S15.** Application of NSM as a versatile anode in Na and K ions storage. (a) Schematic diagram of the NSM-based half-cell. (b) The initial galvanostatic charge/discharge profiles of NSM-based electrodes for SIBs and PIBs at 500 mA g$^{-1}$. (c) Cycle performance of the NSM-based electrodes for SIBs at 500 mA g$^{-1}$. (d) Rate and reproducibility performance of the NSM-based electrodes for SIBs. (e) Cycle performance of the NSM-based electrodes for PIBs at 500 mA g$^{-1}$. (f) Rate and reproducibility performance of the NSM-based electrodes for PIBs.

Figure S13a demonstrates the schematic of SIBs and PIBs. As expected, the ultra-high ICE (90.5%) and ICE (80.1%) for the prepared SIBs and PIBs were realized (Figure S13b). This proves that the conversion reactions with poor reversibility are promoted by Ni NPs:

$$SnO_2 + 4Na^+ + 4e^- \leftrightarrow Sn + 2Na_2O \tag{9}$$

$$SnO_2 + 4K^+ + 4e^- \leftrightarrow Sn + 2K_2O \tag{10}$$
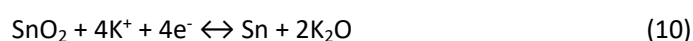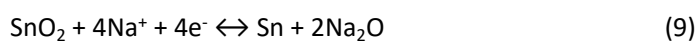
And the discharge capacities of SIBs and PIBs are almost below 2.2 V, which can ensure that NSM can

also be used as a potential anode for Na and K ions storage. In addition, under 500 mA g$^{-1}$, it could deliver the capacities of 552 and 338 mAh g$^{-1}$ in average Na and K ions storage (Figure S13c, S13e). And the stability of the NSM based electrodes during fast ion insertion/extraction process of Na and K battery were performed as shown in (Figure S13d, S13f), even after several charge/discharge cycles at different rates, the reversible specific capacities can be recovered to 599 and 308 mA h g $^{-1}$ for SIBs and PIBs respectively. Further performance displays that NSM can hold the ICE of 88.4% and 78.6% and keep high capacities of 435 and 108 mA h g$^{-1}$ under 1000 mA g$^{-1}$ over 200 cycles for SIBs and PIBs respectively (Figure S14) These results prove that NSM is promising as a multifunctional anode in energy storage. Compared with other structures, NSM shows an enormous breakthrough of ICE in SIBs and PIBs as shown in Figure S13.[4-23]
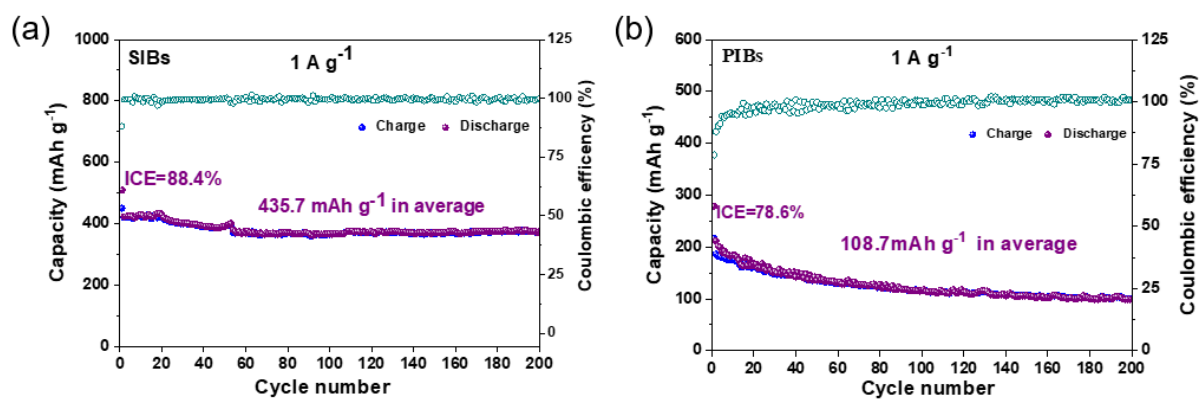
**Figure S16.** Cycle performance of the NSM electrode for (a) SIBs and (b) PIBs at 1000 mA g$^{-1}$.
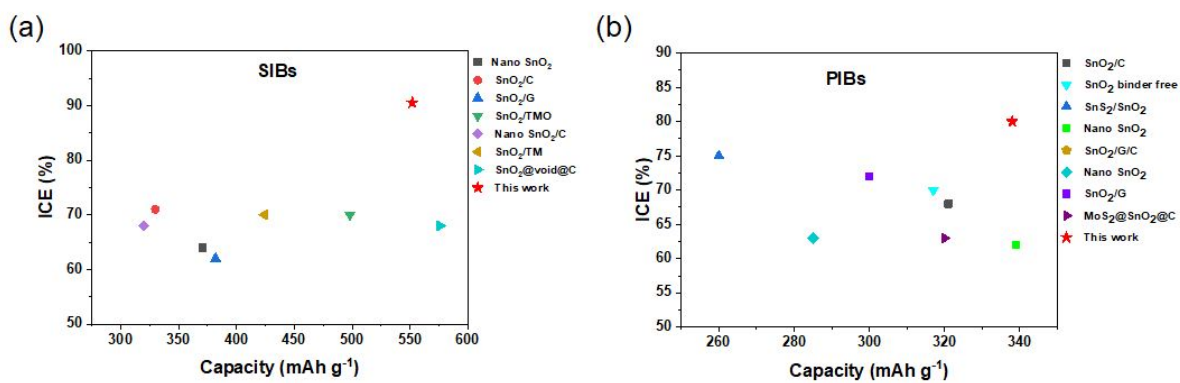
**Figure S17.** (a) The ICEs and capacity of $SnO_2$-based anodes for SIBs reported in the recent literatures, including the nano $SnO_2$[4], $SnO_2$-C[5], $SnO_2$-G[6], $SnO_2$-Metal oxides ($SnO_2$-MOs)[7], $SnO_2$@void@C[5] and $SnO_2$-Metal ($SnO_2$-TMs)[7], (b) for PIBs include the pure nano $SnO_2$[8], $SnO_2$-C[9], $SnO_2$-G[11], $SnO_2$-binder free[15] and $SnO_2$-Metal sulfides ($SnO_2$-MSs)[23].
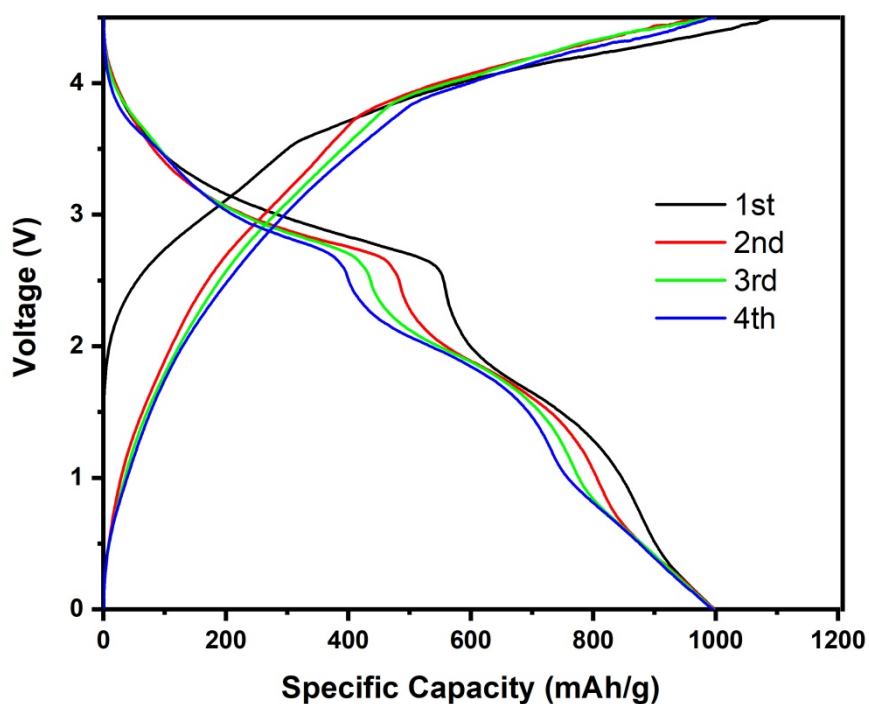
**Figure S18.** Charge-discharge curves of NSM/NCM full cell.

Pre-lithiated $NiO/SnO_2$ (NSM) and $LiNi_{0.8}Co_{0.1}Mn_{0.1}O_2$ (NCM) were utilized as the anode and cathode materials, respectively, for the assembly of a full cell to evaluate its practical application feasibility. Fig. S17 provides supplementary evidence that the full cell also achieve a reversible specific capacity of 1000 mAh $g^{-1}$ (the mass is determined by negative electrode) with an ultrahigh initial coulombic efficiency of 90.72%, demonstrating the possibility of its practical application.

# References

1.  M. Li, J. Li, K. Li, Y. Zhao, Y. Zhang, D. Gosselink and P. Chen, $SiO_2$/Cu/polyacrylonitrile-C composite as anode material in lithium ion batteries, *J. Power Sources* 2013, **240**, 659-666.

2.  C. Hua, X. Fang, Z. Wang and L. Chen, Transition-metal-catalyzed oxidation of metallic Sn in NiO/$SnO_2$ nanocomposite, *Chem.- Eur. J.* 2014, **20**, 5487-5491.

3.  G. Lee, S. Kim, S. Kim and J. Choi, $SiO_2$/$TiO_2$ composite film for high capacity and excellent cycling stability in lithium-ion battery anodes, *Adv. Funct. Mater.* 2017, **27**, 1703538.

4.  R. Biswal, D. Nayak, S. Janakiraman, N. V. P. Chaudhary, S. Ghosh and V. Adyam, Revisiting and enhancing electrochemical properties of $SnO_2$ as anode for sodium-ion batteries, *J. Solid State Electrochem.* 2021, **25**, 561-573.

5.  Y. Liu, X. Fang, M. Ge, J. Rong, C. Shen, A. Zhang, H. A. Enaya and C. Zhou, $SnO_2$ coated carbon cloth with surface modification as Na-ion battery anode, *Nano Energy* 2015, **16**, 399-407.

6.  Y.-X. Wang, Y.-G. Lim, M.-S. Park, S.-L. Chou, J. H. Kim, H.-K. Liu, S.-X. Dou and Y.-J. Kim, Ultrafine $SnO_2$ nanoparticle loading onto reduced graphene oxide as anodes for sodium-ion batteries with superior rate and cycling performances, *J. Mater. Chem. A* 2014, **2**, 529-534.

7.  J. Wang, G. Zhu, X. Liu, G. Wang, H. Wang and J. Bai, In situ synthesis of tin dioxide submicrorods anchored on nickel foam as an additive-free anode for high performance sodium-ion batteries, *J. Colloid Interface Sci.* 2019, **533**, 733-741.

8.  M. Shimizu, R. Yatsuzuka, T. Koya, T. Yamakami and S. Arai, Tin oxides as a negative electrode material for potassium-ion batteries, *ACS Appl. Energy Mater.* 2018, **1**, 6865-+.

9.  H. Qiu, L. Zhao, M. Asif, X. Huang, T. Tang, W. Li, T. Zhang, T. Shen and Y. Hou, $SnO_2$ nanoparticles anchored on carbon foam as a freestanding anode for high performance potassium-ion batteries, *Energy Environ. Sci.* 2020, **13**, 571-578.

10. Q. Zhu, P. Wu, J. Zhang, W. Zhang, Y. Zhou, Y. Tang and T. Lu, Cyanogel-derived formation of 3D nanoporous $SnO_2$-$M_xO_y$ (M= Ni, Fe, Co) Hybrid Networks for High-Performance Lithium Storage, *Chemsuschem* 2015, **8**, 131-137.

11. Z. Huang, Z. Chen, S. Ding, C. Chen and M. Zhang, Enhanced conductivity and properties of $SnO_2$-graphene-carbon nanofibers for potassium-ion batteries by graphene modification, *Mater. Lett.* 2018, **219**, 19-22.

12. Z. Huang, Z. Chen, S. Ding, C. Chen and M. Zhang, Enhanced electrochemical properties of $SnO_2$-graphene-carbon nanofibers tuned by phosphoric acid for potassium storage, *Nanotechnology* 2018, **29**, 375702.

13. S. Luo, T. Wang, H. Lu, X. Xu, G. Xue, N. Xu, Y. Wang and D. Zhou, Ultrasmall $SnO_2$ nanocrystals embedded in porous carbon as potassium ion battery anodes with long-term cycling performance, *New J. Chem.* 2020, **44**, 11678-11683.

14. X. Shi, S. Pei, F. Zhou, W. Ren, H.-M. Cheng, Z.-S. Wu and X. Bao, Ultrahigh-voltage integrated micro-supercapacitors with designable shapes and superior flexibility, *Energy Environ. Sci.* 2019, **12**, 1534-1541.

15. G. Suo, D. Li, L. Feng, X. Hou, Y. Yang and W. Wang, $SnO_2$ nanosheets grown on stainless steel mesh as a binder free anode for potassium ion batteries, *J. Electroanal. Chem.* 2019, **833**, 113-118.

16. Z. Kong, X. Liu, T. Wang, A. Fu, Y. Li, P. Guo, Y.-G. Guo, H. Li and X. S. Zhao, Three-dimensional hollow spheres of porous $SnO_2$/rGO composite as high-performance anode for sodium ion batteries, *Appl. Surf. Sci.* 2019, **479**, 198-208.

17. Z. Wang, K. Dong, D. Wang, S. Luo, Y. Liu, Q. Wang, Y. Zhang, A. Hao, C. Shi and N. Zhao, Ultrafine $SnO_2$ nanoparticles encapsulated in 3D porous carbon as a, high-performance anode material for potassium-ion batteries, *J. Power Sources* 2019, **441**, 227191.

18. L. Fang, N. Bahlawane, W. Sun, H. Pan, B. B. Xu, M. Yan and Y. Jiang, Conversion-alloying anode materials for sodium ion batteries, *Small* 2021, **17**, 2101137.

19. R. Li, G. Zhang, Y. Wang, Z. Lin, C. He, Y. Li, X. Ren, P. Zhang and H. Mi, Fast ion diffusion kinetics based on ferroelectric and piezoelectric effect of $SnO_2/BaTiO_3$ heterostructures for high-rate sodium storage, *Nano Energy* 2021, **90**, 106591.

20. D. Narsimulu, G. Nagaraju, S. C. Sekhar, B. Ramulu and J. S. Yu, Three-dimensional porous $SnO_2$/carbon cloth electrodes for high-performance lithium- and sodium-ion batteries, *Appl. Surf. Sci.* 2021, **538**, 148033.

21. G. M. Tomboc, Y. Wang, H. Wang, J. Li and K. Lee, Sn-based metal oxides and sulfides anode materials for Na ion battery, *Energy Storage Mater,* 2021, **39**, 21-44.

22. Z. Chen, D. Yin and M. Zhang, Sandwich-like $MoS_2/SnO_2$/C with High Capacity and Stability for Sodium/Potassium Ion Batteries, *Small* 2018, **14**, 1703818.

23. G. Suo, D. Li, L. Feng, X. Hou, X. Ye, L. Zhang, Q. Yu, Y. Yang and W. Wang, Construction of $SnS_2/SnO_2$ heterostructures with enhanced potassium storage performance, *J. Mater. Sci. Technol.* 2020, **55**, 167-172.